

Turbulence under spilling breakers using discrete wavelets

S. Longo

Abstract Measurements of the kinetic energy of turbulence under spilling waves have been analysed using orthogonal wavelets. Data have been collected using 2-D laser Doppler velocimetry for pre-breaking regular waves, generated in a wave tank. The contribution of different scale vortices is computed, and also phase resolved. It is found that micro-vortices ($2 \text{ mm} < l < 0.10 \text{ m}$ for the tested case) and mid-size vortices ($0.10 \text{ m} < l < 4.0 \text{ m}$ for the tested case) are generally dominant, carrying more than 70% of the total turbulence energy under the wave crest. The phase resolved energy spectra are computed, which allows the computation of the transverse and of the longitudinal correlations.

List of symbols

\sim	phase or ensemble average operator
\wedge	phasic average operator
-	time average operator
$\langle \dots \rangle$	ensemble average
$\alpha \sim 3\alpha_1$	Kolmogorov constant
γ, γ_{jk}	function
ρ	mass density (kg/m^3)
ν	kinematic fluid viscosity (m^2/s)
Λ	integral length scale of turbulence (m)
ΔT_i	time interval (s)
λ_E	Taylor length micro-scale (m)

ϵ	turbulent energy dissipation rate (m^2/s^3)
κ	turbulent kinetic energy (m^2/s^2)
ξ	translation parameter
τ_E	Eulerian time micro-scale (s)
τ	shear stress (Pa)
η_K	Kolmogorov length micro-scale (m)
$A_j(x)$	approximation at level j
a	dilation parameter
C	wave celerity (m/s)
$D_j(x)$	detail at level j
DWT	discrete wavelet transform
$E_1(k_1), E_2(k_1)$	energy spectrum in the wave-number domain (m^3/s^2)
$E_1(f)$	energy spectrum in frequency domain (m^2/s)
f	frequency (Hz), function
f_{acq}	sampling frequency (Hz)
g	gravitational acceleration (m/s^2)
h	local water depth (m)
H	wave height (m)
k, k_1	wave number (m^{-1})
$k_{\text{min}}, k_{\text{max}}$	minimum, maximum wave number
k_d	dissipative wave number (m^{-1})
\mathbf{k}	wave number (vector) (m^{-1})
l	length scale (m)
LDV	laser Doppler velocimetry
N	number of samples
N	number of levels in wavelet decomposition
PIV	particle image velocimetry
$R_E(r)$	normalised Eulerian space autocorrelation
$R_E(\tau)$	normalised Eulerian time autocorrelation
Re_λ	Reynolds number based on Taylor micro-scale
s_{ij}	fluctuating rate of strain (s^{-1})
STFT	short time Fourier transform
T	wave period (s)
T_m	period of time averaging (s)
TFR	time frequency representation
t, t_k, t', τ	time variable (s)
T_E	time macro-scale of turbulence (s)
\bar{u}	mean velocity
u', v'	fluctuating velocity (m/s)
\tilde{u}, \tilde{v}	organised fluctuating velocity (m/s)
U, V, W	velocity scales, velocity components (m/s)
u	turbulence scale (m/s)
\mathbf{u}	velocity vector (m/s)
VITA	variable interval time average
w_{jk}	wavelet coefficients
x, y, z, x_i	spatial co-ordinates (m)

Received: 5 October 2001 / Accepted: 30 August 2002
 Published online: 23 November 2002
 © Springer-Verlag 2002

S. Longo
 Dipartimento di Ingegneria Civile,
 Università degli Studi di Parma,
 Parco Area delle Scienze, 181/A, 43100 Parma, Italy
 E-mail: slongo@unipr.it
 Tel.: +39-0521-905157
 Fax: +39-0521-905924

This work is undertaken as part of Italy–Spain Co-operation Project 1999–2000, funded by MURST of Italy and of Spain. It has been also partly supported by the MAST III–SASME Project (“Surf and Swash Zone Mechanics”) funded by the Commission of the European Communities, Directorate General Research and Development under contract No. MAS3-CT97–0081. I wish to express many thanks to the technicians and to the staff of the Ocean and Coastal Research Group Laboratory, in Santander, for their valuable collaboration in carrying out experiments. The manuscript was written during my visit to the Université de Bretagne Occidentale in Brest, France, where I was kindly hosted by Prof. Le Guen. I also thank Tim Chesher for kindly polishing my English.

Introduction

Turbulence following the breaking of waves in the surf zone is a widely studied phenomenon, both numerically and experimentally. Wave breaking is characterised by a strong generation of vorticity, which is always followed by a huge amount of turbulence generated near the free surface. Often, but not necessarily always, strong free surface turbulence entraps air bubbles. The turbulence is then convected and diffused and reaches the bottom in shallow water, lifting and trapping sediments. At the same time a smaller amount of vorticity and turbulence is also generated near the bottom.

The difficulties in modelling such a complicated flow field, have pushed many researchers to investigate possible similarities with better known and simpler flow fields, carrying out several experiments in order to validate their models. Several models of wave breaking include some well-known turbulent structures such as mixing layers, hydraulic jumps, and submerged jets. As Svendsen and Putrevu (1995) pointed out, turbulence under breaking waves is different from any other form of turbulent flow.

Many experiments were dedicated to measuring the detailed structure of the turbulent flow field in a breaker, using LDA or hot films in 2-D arrays, with few attempts to measure 3-D velocity components. Svendsen (1987) compared different sets of experiments from Stive (1980), Nadaoka and Kondoh (1982), Hattori and Aono (1985), and the numerical model results of Deigaard et al. (1986). He concluded that turbulence energy variation in time and in the vertical is almost negligible.

Cox et al. (1994) investigated turbulence under spilling breakers and concluded that assuming local equilibrium is a reasonable approximation in the inner surf zone.

Ting and Kirby (1994, 1995, 1996), carried out several experiments analysing turbulence in spilling and plunging breakers, the former showing a larger time variation than the latter. The turbulence dies out between successive breakers. Ting and Kirby carefully analysed and quantified the mechanisms of generation and transport of turbulence and the energy budget.

In addition, PIV results are available (Dabiri and Gharib 1997), sometimes with high image density (Lin and Rockwell 1994). See Chang and Liu (1998) and Greated and Emarat (2000) for experiments on breaking waves through PIV.

It is common to describe turbulent fields as a mixture of eddies at different scales, often referred to as coherent structures. Some experiments have clearly confirmed the existence of such classes of eddies in breaking waves (Nadaoka et al. 1989; Chang and Liu 1998), with the appearance of oblique vortices. In general, the flow field under breaking waves is strongly inhomogeneous. The larger eddies have sizes comparable with the scale of inhomogeneity of the flow (wavelength, breaker height); the smaller eddies act in a locally homogeneous flow. All concepts developed in isotropic turbulence analysis can be used essentially for the latter eddies, depending on the shear rate due to the mean motion and to the macro-vortices, whereas a complete analysis of inhomogeneous and

non-isotropic turbulence is not yet possible. Moreover a large degree of intermittency is expected at all scales. Turbulence generation is an intermittent phenomenon, but also dissipation seems to be organised in patches, instead of being uniformly present in the flow field. The measurements by George et al. (1994) confirm that dissipation in the surf zone is an intermittent process following a lognormal distribution (Kolgomorov 1962; Obukhov 1962). The connection between coherent structures and intermittence is an important aspect of turbulence modelling. According to many researchers, coherent structures generate most of the turbulent shear stress, even in homogeneous turbulence. The main effect of disregarding the presence (or the effects) of these families of eddies, is the poor adherence to reality of some common assumptions, such as the eddy viscosity concept to express the behaviour of the turbulence stresses in terms of the mean velocity gradients.

The first question (without a clear answer) is: what is turbulence in unsteady flows. Then how is it possible to separate turbulence and mean flow? Different methods to extract turbulence in unsteady flows have been proposed by several Authors (Thornton 1979; Nadaoka and Kondoh 1982; Sakai et al. 1982; Hattori and Aono 1985; George et al. 1994; Rodriguez et al. 1999; Petti and Longo 2001). There is no doubt that the results of experimental data analysis are strongly affected by the assumption behind the technique of extracting the turbulence.

The technique for analysing turbulence is also not unique. Time series analysis and, in particular, turbulence analysis has taken advantage of Fourier transforms using harmonic sine-cosine function space as a basis, especially since algorithms such as fast Fourier transform became available for numerical applications. Instead of listing the numerous and unquestionable advantages in using Fourier transform, we prefer to provide evidence of the limitations caused by the classical sine-cosine basis. Sine and cosine are periodic functions spreading all over the space or time domain, whereas all time series (or space series) are necessarily limited. Using the sine-cosine basis, frequency information refers to the complete duration of a signal and a contribution arising from a local oscillation or local structure in the time series (or space series) is spread all over the transform, without carrying information on its location on time or space axis. This is in contrast with the need for a proper detection of time location of specific coherent structures, which is almost always present in time series of turbulence velocity. An attempt to overcome these limits is the work of Gabor (1946), who adapted the Fourier transform by analysing only small windows of the signal (STFT) and obtained a representation of a time series in a frequency-time domain. The limit of Gabor's approach is in the choice of the size of the window amplitude, which is usually constant independent of the frequency and on the large bandwidth, which in turn reduces frequency resolution and estimate accuracy (see Newland 1993). Also, Wigner (1932) and Ville (1948) developed and applied an analysis of short data windows using Fourier transforms with classical harmonic functions as the basis, which was further implemented as a TFR, but they did not

overcome the limit of the continuing nature of harmonic waves, so the waves were unable to decompose a short time signal efficiently. Moreover the TFR representation is non-unique, requiring careful design of the algorithms.

An alternative method of signal analysis has been developed during the 1980s and 1990s to present, using formal concepts from the beginning of the 20th century, and is based on classical Fourier decomposition using local orthogonal functions as basis. It is called wavelet analysis. Wavelet analysis is widely used in image compression, voice identification, signal transmission and has become an important tool for intermittent, self-similar, complex signals, especially in extracting local structures and singularities (see Farge 1992; Fofoula-Georgiu and Kumar 1994; and Liu 2000 for reviews; Camussi and Guj 1997). The cascade models in turbulence rely on the assumption that energy density is segmented in the wave-number domain and is exchanged between elementary individual eddies, and hence wavelet analysis appears to have the potential to reveal such eddies.

2

Scope and objectives

The aim of the present experimental work is to provide information on turbulence structure and spectra in a typical unsteady flow as waves. The present analysis refers to experiments on spilling breakers in a wave flume, with LDV 2-D measurements taken in the immediately pre-breaking section. The velocity signal is periodic and turbulence is superimposed with varying intensity and scale structure depending on the phase. A wavelet-based algorithm is used to decompose turbulence energy into contributions at different frequencies (wave numbers) and different locations on the time axis.

In Sect. 3 a short description of the experiments is given and Sect. 4 provides a classical time domain analysis of the results. In Sect. 5 a short introduction to wavelet theory is given, in order to recall some important properties necessary for quantitative assessment of the results. In Sect. 6 the scale analysis in turbulence fields is revisited. The application of wavelet theory to data analysis and discussion of the results is given in Sect. 7.

3

The experiments

The experiments were carried out in the small flume in the laboratory of the Ocean and Coastal Research Group at the Universidad de Cantabria in Santander, Spain. The flume is 24-m long, 0.58-m wide and 0.8-m deep and has glass sidewalls and bottom (Fig. 1). The wave generator has a paddle with an active absorption system in order to correct for reflected waves. A false acrylic glass bottom was installed in the wave tank, creating a uniform slope 1:20

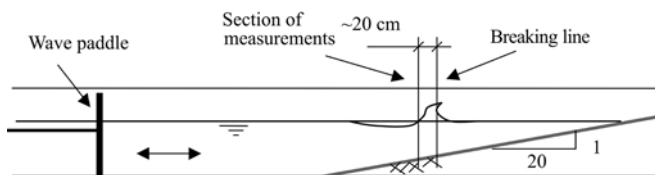


Fig. 1. Layout of the flume

starting 8.0 m from the paddle. A detailed description of the experiments is presented in Longo et al. (2001).

A 2-D laser Doppler velocimeter was used for velocity measurements, which works by a process of backscatter using optical fibres to transfer a laser signal. It is a two-colours, four-beams system with a 6 W laser generator. The Doppler frequency information was logged by a counter and stored in a PC. No specific seeding was necessary, even though a small quantity of TiO_2 ($0.2 \mu\text{m}$) that was used as tracer for ultrasound instruments was still present in the water. The expected error in velocity measurements is 1% of the velocity range. The test refers to a 5th order regular wave over a period equal to $T=3.0$ s and $H=10$ cm with a still water level (swl) in front of the paddle equal to 37 cm. The wave breaks as a spilling breaker. Velocity measurements were carried out at 21 points in the vertical at a single section 13.0 m from the paddle in the sloping bottom part of the tank, with a still water level $h=12$ cm. The measurement section is just before the breaking wave, in order to limit the air bubble content and also to allow LDV measurements in part of the crest. The first measurement point is that nearest to the bottom. Other measurement points are equally spaced at 10 mm up the vertical. Nineteen of these measurement points were suitable for further analysis, which covers more than half of the crest. The measurements lasted for 300 s at each level (100 wave cycles) and a data rate variable was used during the wave period because it relates to the number of validated bursts per unit time, which varies. In order to obtain time series with a constant time step, the data have been linearly interpolated at 2 kHz, which is $\sim 20\%$ higher than the mean frequency acquisition data rate. On average, the response of the system is satisfactory up to 1.6 kHz.

4

Data analysis in the time domain: extracting turbulence

The raw velocity data have to be averaged in order to extract the mean value and the fluctuating component. There are several techniques used and operators available for averaging (see Longo et al. (2002), for a review). The average operator most used in periodic signals is the ensemble or phase average operator, defined as:

$$\tilde{U}(t) = \frac{1}{N} \sum_{k=0}^{N-1} U(t + kT) \quad 0 \leq t < T \quad (1)$$

where U is the instantaneous value, N is the number of cycles and T is the period. If the period is slightly fluctuating (as usually happens in well-controlled wave tanks also) the ensemble average distorts and dampens the average. If a well-identified trigger is available, it is possible to apply the conditional average, also called variable interval time average (VITA):

$$\tilde{U}(t) = \frac{1}{N} \sum_{k=0}^{N-1} U(t + t_k) \quad 0 \leq t < \min(T) \quad (2)$$

where t_k is the instant of trigger of the k -cycle and $\min(T)$ is the minimum time period in the series of N cycles. Because the time period of each cycle ($t_k - t_{k-1}$) is not constant, it is appropriate to stretch the data before averaging in order to

extend the cycle all over the mean period. Abnormal varying periods can also be eliminated in the analysis.

Another operator is the moving average, defined as:

$$\overline{U(t)} = \frac{1}{T_m} \int_{t-T_m/2}^{t+T_m/2} U(t') dt' \quad (3)$$

where T_m is the period of time averaging. The moving average becomes the standard time average if the integral extends all over the time series.

If the measurement point is out of the water during part of the time series, we can define a phasic average:

$$\hat{U} = \frac{\sum_i \int_{\Delta T_i} U(t) dt}{\sum_i \Delta T_i} \quad (4)$$

where ΔT_i represents the time steps when wet.

In the analysis of the present data the VITA technique was used and hereafter the terms phase average stand for

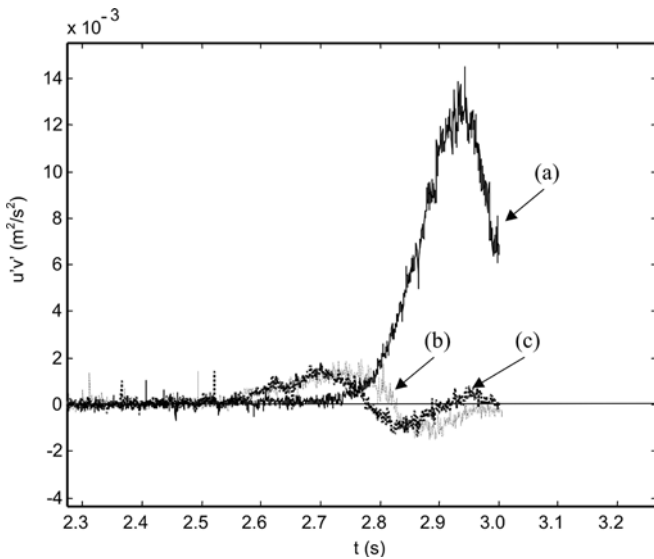


Fig. 2. Reynolds stress computed using: a phase average with period $T=3.0$ s; b phase average with period $T=3.005$ s; c VITA

VITA. The trigger instant was obtained by (a) performing a moving average of the horizontal velocity signal using $T_m=0.2$ s; (b) selecting the instant of maximum horizontal velocity in the moving time-averaged series as the trigger (value of t_k). The chosen value of $T_m=0.2$ s is the value that minimises the variation in trigger instant (increasing T_m does not significantly modify the trigger instant). The resulting periods (t_k-t_{k-1}) are very stable and uniform, with a value of $T=3.0\pm 0.05$ s for a 95% confidence band. Only those periods in the confidence band were used in computing the phase-averaged horizontal velocity, resulting in $\sim 90\%$ of useful periods. Each time series lasts for 300 s, resulting in ~ 80 useful periods. The trigger times used for computing the horizontal velocity average were also used for computing the vertical velocity average. Similar computations were carried out to extract the turbulence components and Reynolds' stress $-\overline{u'v'}$.

The adoption of a standard phase average includes subharmonics in turbulence, a general dampening of the computed mean flow velocity and a macroscopic increment of turbulence, as shown in Fig. 2, where Reynolds stress at $z=20$ mm is plotted as obtained by phase averaging with slightly varying period ($T=3.0$ s and $T=3.005$ s) and also applying VITA.

The phase-averaged velocity vectors are presented in Fig. 3. On the right panel the mean velocity and the mean phasic velocity are also reported. The undertow current (a seaward gravity driven current related to wave set-up) reaches a maximum value equal to $\sim 0.1C$, where $C = \sqrt{gh}$ is the wave celerity.

The vertical distributions of vorticity and shear rate are presented in Fig. 4. The mean values are negligible below the wave trough, and increase strongly in the wave crests, where most vorticity and turbulence is generated. Since only two velocity components are measured, vorticity is intended as the component of the vector vorticity normal to the plane of main motion. Also the shear rate refers to rate of deformation in the plane of main motion.

In Fig. 5 the mean values of the two measured turbulent components are presented as non-dimensional with

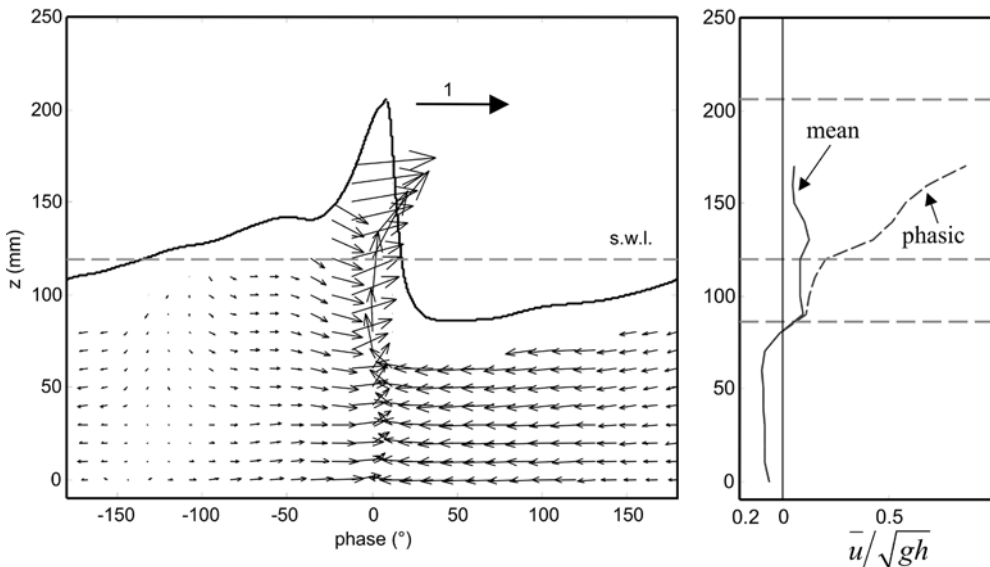


Fig. 3a, b. Phase average velocity. a Vector modulus indicated is $|u|/\sqrt{gh}$; b mean and phasic average velocity in the vertical. Undertow is evident below the trough

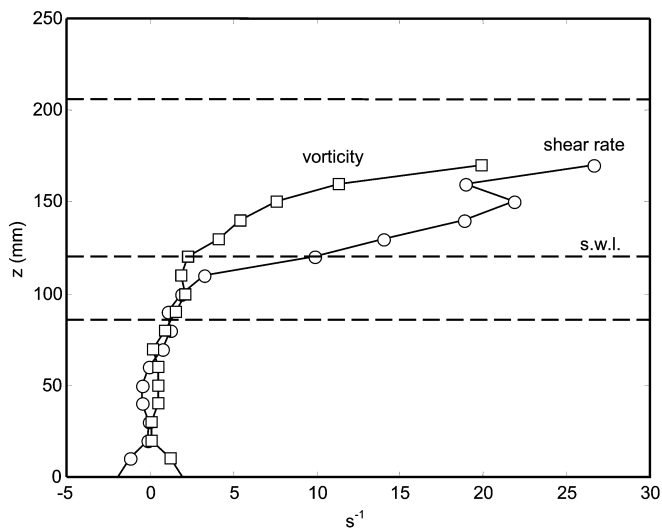


Fig. 4. Mean vorticity and mean shear rate. Phasic average

respect to local wave celerity. In order to improve visualisation of the high-energy spot caused by breaking, the phasic average is also shown in the crest. Figure 6 shows the phase variation of turbulent energy components averaged in the vertical.

The results are comparable with results of other research (e.g. see Svendsen (1987) for a comparison among data by different authors); nevertheless anisotropy is quite evident particularly near the bottom. The mean ratio between the components v^2/u^2 is equal to ~ 0.38 below the trough level and to ~ 0.41 when also considering the wave crest. These values are typical of open channel flows and boundary layers (see Townsend 1976; Svendsen 1987). Also Ting and Kirby (1996) reported the mean ratio v^2/u^2 for spilling and plunging waves in several sections after breaking. Present results are more similar to those obtained by Ting and Kirby for plunging breakers, with a linear increment starting from the bottom.

In the crest, vertical turbulence is stronger than horizontal turbulence.

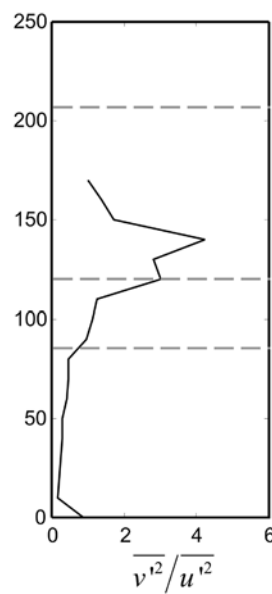
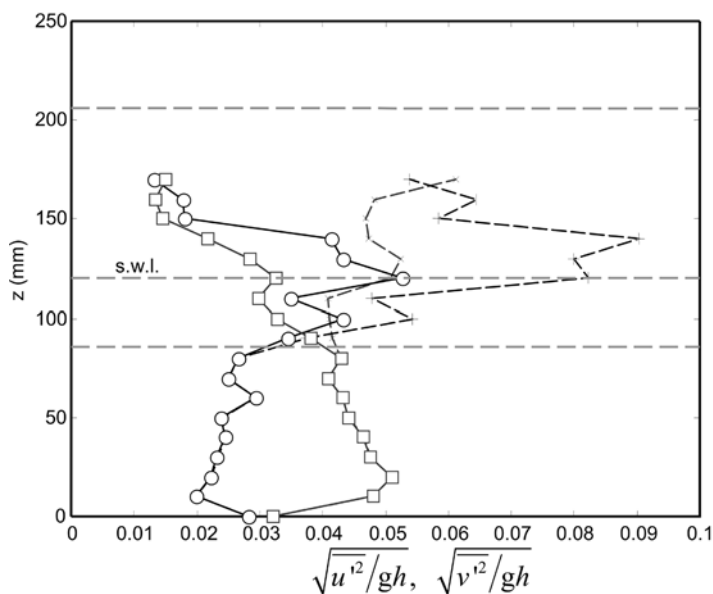


Fig. 5. a Vertical variation of horizontal (open square) and vertical (open circle) turbulence intensity. Thin lines are phasic averages. b ratio between vertical and horizontal turbulent components

5 Wavelet theory

Wavelet analysis is a tool for mapping a function space onto a different domain. A wavelet is a waveform of limited duration and zero average. If $\varphi(x)$ is the basic wavelet (mother wavelet), a set of wavelet functions is obtained through dilation and translation:

$$\{\varphi_{a,\xi}\} = \varphi\left(\frac{x-\xi}{a}\right) \tag{5}$$

where a is a dilation parameter and ξ is a translation parameter. If a is discrete variable, the set $\{\varphi_{a,\xi}\}$ can be built up in order to be an orthonormal basis, able to describe a complete space function and to give an accurate decomposition of any function in the same space.

By letting $a=2^{-j}$ and $\xi=k2^{-j}$, the general form of the orthonormal basis in Eq. (5) is:

$$\{\varphi_{jk}\} = \varphi(2^jx - k) \tag{6}$$

Given a signal $f(x)$, its DWT is defined as:

$$w_{jk} = 2^{j/2} \int_{-\infty}^{+\infty} f(x)\varphi * (2^jx - k)dx = 2^{j/2} \int_{-\infty}^{+\infty} f(x)\varphi_{*jk}dx \tag{7}$$

where the asterisk indicates complex conjugate.

The use of orthonormal wavelets induces a discrete finite resolution and localisation, but allows an exact reconstruction of the signal as:

$$\begin{aligned} f(x) &= \sum_{j,k} w_{jk}\varphi_{jk}(x) = \bar{f} + \sum_{j=0}^{(\log N)/(\log 2)} \sum_{k=0}^{2^j-1} w_{jk}2^{j/2}\varphi(2^jx - k) \\ &= \bar{f} + \sum_{j=0}^{(\log N)/(\log 2)} D_j(x) \end{aligned} \tag{8}$$

where \bar{f} is the mean value of the signal.

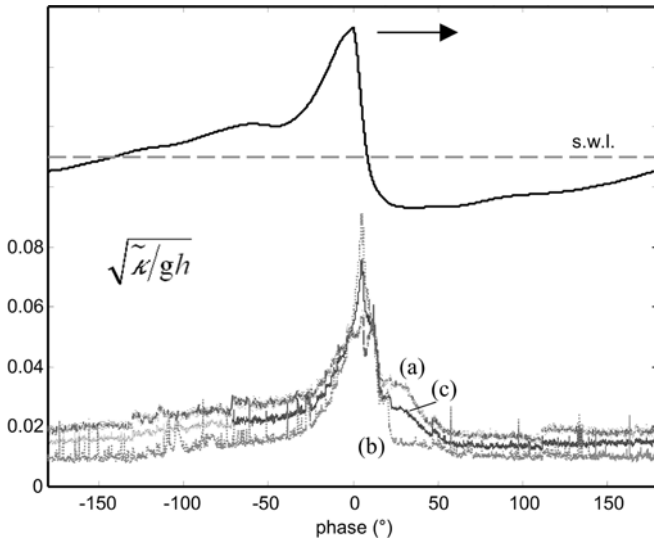


Fig. 6. Phase variation of: a horizontal turbulence; b vertical turbulence intensity; c total turbulence energy. Mean values in the vertical, non-dimensional respect to wave celerity

Fixing a maximum level J for details, the function $f(x)$ can be written as:

$$f(x) = \bar{f} + \sum_{j>J} D_j(x) + \sum_{j=0}^J D_j(x) = \bar{f} + A_j(x) + \sum_{j=0}^J D_j(x) \quad (9)$$

with $A_j(x) = \sum_{j>J} D_j(x)$. $A_j(x)$ is called approximation at level j and contains the coarser information on $f(x)$.

Practical use of Eq. (8) for computing the coefficients became possible thanks to the development of the algorithm DWT by Mallat (1989).

Using orthogonal properties, it is possible to demonstrate that (see Newland 1993, p. 348):

$$\int_0^1 f^2(x) dx = \bar{f}^2 + \sum_{j,k} w_{jk}^2 \left(\frac{1}{2^j} \right) \quad (10)$$

This relation shows that the mean square (generally called energy) of the signal is distributed in a precise and computable way among different wavelet components. The interval of integration has been compressed into $[0-1]$ because it is assumed that wavelet functions are wrapped round the interval $0 < x < 1$. The wavelet power spectrum at a specific scale is the weighted average of the Fourier power spectrum over frequencies at that scale (Hudgins 1992). Moreover at level j there are 2^j wavelets in the unit interval, spaced $1/2^j$ apart with a fundamental frequency of 2^j cycles per unit interval. This makes it possible to associate a frequency (in the time domain) or a wave number (in the space domain) to each level j . In the case of orthogonal dyadic wavelets, the fundamental frequencies (or wave numbers) increase in octaves.

There are several mother functions that satisfy the orthonormality and for which DWT algorithms are available. The choice of a specific family is dictated by the aim of the transform. Hajj (1999) and Hajj et al.

(2000) used Daubechies orthonormal wavelets to examine energy level and intermittence of turbulence scales in atmospheric wind and in wind tunnel experiments respectively. Kaspersen and Krostad (2001) used a ‘‘Mexican hat’’ wavelet for burst detection in turbulence. Gilliam et al. (2000) used a Morlet wavelet for coherent structure detection.

In the present analysis we use Daubechies fourth order wavelet (Fig. 7), but results are similar using different wavelet families.

6 Scale analysis

Before applying wavelet decomposition, we recall some scale concepts in turbulence. A classical interpretation of turbulence is the cascade mechanism (Tennekes and Lumley 1972; Hinze 1975), with energy contained at large scales (small wave number, essentially related to the geometry of the flow field) transferred to small scales (large wave number) where it is turned into heat by viscosity. Two commonly used length scales are due to Taylor, who expressed the integral length scale Λ based on the spatial correlation function:

$$\Lambda = \int_0^{\infty} R_E(r) dr \quad (11)$$

where:

$$R_E(r) = \frac{\langle u'(x)u'(\widetilde{x+r}) \rangle}{\langle u'^2(x) \rangle} \quad (12)$$

is the normalised Eulerian spatial correlation function for homogenous and isotropic turbulence.

Referring to experiments, it is usually easier to measure fluid velocities at a single point obtaining a time series of the local velocity, which leads to the Eulerian time correlation (also normalised):

$$R_E(\tau) = \frac{\langle u'(t)u'(\widetilde{t+\tau}) \rangle}{\langle u'^2(t) \rangle} \quad (13)$$

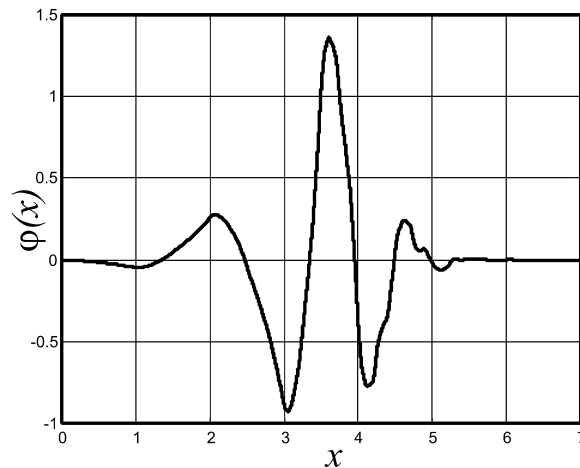


Fig. 7. Fourth order Daubechies wavelet

Consequently the Eulerian integral time scale is defined as:

$$T_E = \int_0^{\infty} R_E(\tau) d\tau \quad (14)$$

i.e. the area under the time autocorrelation function, assumed as the duration of the macro-vortices. The transformation of the integral time scale into the integral length scale can be carried out assuming Taylor's hypothesis of "frozen turbulence", which is briefly discussed in the following section.

Our measurements and most of the experimental measurements in turbulence are in the time domain, with a probe (LDV, hot film, etc.) fixed in space and able to collect a time series of fluid velocity. Most of turbulence theories refer to wave number instead of frequency, and transformation is necessary. The widely used transformation relies on Taylor's approximation, which neglecting all terms in the balance of momentum, except the fluid acceleration, states that:

$$\frac{\partial}{\partial t} \approx -U \frac{\partial}{\partial x} \quad (15)$$

where U is a proper velocity scale and the other two velocity components, V and W , have been assumed negligible and $u \ll U$, with u the scale of turbulence (u/U less than ~ 0.1 and is better satisfied at a high wave number, see McComb (1991)).

The correspondent transformation is:

$$\frac{f}{U} = \frac{|\mathbf{k}|}{2\pi} = \frac{k}{2\pi} \quad (16)$$

where k is the modulus of the wave number.

We have applied Taylor's hypothesis assuming as a velocity scale the modulus of the local phase-averaged velocity. It generally results in satisfying $(u/U) < 0.1$ except during flow inversion (almost zero fluid velocity and relatively high turbulence velocity scale). To overcome the singularity, the time interval of averaging the variables has been locally increased during inversion.

Taylor's time micro-scale is defined as the interception of the time axis with the parabola osculating the auto-correlation function in its vertex:

$$\tau_E = \sqrt{\frac{-2}{[d^2 R_E / dt^2]_{t=0}}} \quad (17)$$

and then is converted into Taylor's length micro-scale:

$$\lambda_E = U \tau_E \quad (18)$$

The importance of Taylor length micro-scale is due to its relation with the rate of dissipation of energy ϵ , that in isotropic turbulence is (Batchelor 1953):

$$\epsilon = 2\nu \overline{s_{ij} s_{ij}} \simeq \frac{15\nu \langle \widetilde{u'^2} \rangle}{\lambda_E^2} \quad (19)$$

s_{ij} is the fluctuating rate of strain. The above equation is substantially accurate because at the scale of dissipation at

large Reynolds numbers the structure of turbulence is nearly isotropic. The rate of dissipation, using a dimensional concept, allows the Kolmogorov length scale of dissipation to be defined as $\eta_K \equiv (\nu^3/\epsilon)^{1/4}$, which is evaluated assuming that most energy is dissipated by viscosity acting efficiently in dampening micro-vortices.

It is also possible to compute the rate of dissipation by integrating the dissipative spectrum.

The macro length scale and the Kolmogorov length micro-scale bound the range of the wave number, with a minimum wave number:

$$k_{\min} = \frac{2\pi}{\Lambda} \quad (20)$$

and a maximum wave number k_d conventionally assumed equal to the inverse of the length scale of dissipation:

$$k_d = \frac{1}{\eta_K} \quad (21)$$

A rough computation, assuming a velocity scale equal to $\sqrt{\bar{k}}$ and the computed Taylor length micro-scale equal to ~ 0.2 mm, gives

$$k_{\max} = k_d = 5 \times 10^3 \text{ m}^{-1}.$$

7

Data analysis using wavelets

Turbulence extracted using the technique described in Sect. 4, has been further analysed using Daubechies fourth order wavelets (the mother structure of which is drawn in Fig. 7). The results are not largely dependent on the type of wavelet. The length of the analysed sample is 2^{19} points, corresponding to $\cong 262$ s at 2 kHz sampling rate. The maximum number of scales allowed is $N=16$.

The wavelets used are localised in time but not in frequency. Their frequency resolution is roughly related to the level j , depending on the shape of the wavelet. The scale is related to level j by $a=2^j$. The higher the level (the scale), the lower the time resolution (and the higher the frequency). The frequency range covered by the j -level wavelet applied to a time series sampled at f_{acq} can be evaluated as $[f_{\text{acq}}2^{-j-1} - f_{\text{acq}}2^{-j}]$. The frequency covered by the decomposition has an upper limit equal to $f_{\text{acq}}/2$, and a lower limit equal to $f_{\text{acq}}/2^{(N+1)}$. In the present experiments, level 1 covers the frequency range [500, 1,000] Hz and the maximum allowed level covers the frequency range [0.015, 0.03] Hz. The coarser details are included in the approximation A_{16} .

Considering that the data rate at 2 kHz has resulted in oversampling of the available data set, in order to have a constant Δt , and that (especially in the measuring points far from the bottom and near the free surface) the effective data rate is smaller, due to the presence of strong disturbances, the level 1 wavelet (maximum frequency) is not very representative and its energy is always a negligible. Moreover using Taylor's hypothesis of frozen turbulence, a low velocity scale maps the higher frequency into a very small length scale, but the minimum value of the length

scale has to be of the order of the volume of measurements of the laser system, which is less than 1 mm.

Having computed the wavelet coefficients using DWT, the mean energy contribution associated with the i -phase in the period was calculated using Eq. (10), summing only the square coefficients in the i -phase interval. Moreover, extending the summation only to some levels of the DWT, it is possible to evaluate only that energy associated with a specific range of frequency (or wave number).

In order to have a clear look at the kinetic turbulent energy budget, we first need to define some relevant scales. Considering the nature of the flow field, we can assume that the length of the wave defines the size scale of a periodic macro-vortex filling the system with energy. The wave height near the breaking point is also an important

length scale. We finally assume that the dissipation range is limited by $10^{-1}k_d$. Hereafter we use the terms “macro-vortices” for those vortices with a length scale greater than the length of the wave, $l > 4.0$ m, “mid-size vortices” as those in the range $0.10 \text{ m} < l < 4.0 \text{ m}$, i.e. between the breaker height and the wave length, micro-vortices as those vortices in the range $2 \times 10^{-3} \text{ m} < l < 0.10 \text{ m}$ and “dissipative vortices” as those in the range $l < 2 \times 10^{-3} \text{ m}$. This classification is slightly different from the common classification, which separates macro-vortices, energy-containing vortices and dissipative vortices.

The computed distribution in the vertical (Fig. 8) shows that the macro-vortices carry a few per cent of the total energy, more or less uniformly in the vertical. Their energy drops to zero in the wave crest, for clear physical limitations. Dissipation vortices increase toward the bottom and in the wave crest, where most generation takes place followed by strong local dissipation. The micro-vortices share the global energy with the mid-size vortices. In the crest they carry the relevant energy, which almost doubles the mean energy present below the trough.

The phase distribution of turbulent energy at the different scales is also shown in Fig. 9. Macro-vortices also appear uniformly at different phases, and represent a base contribution of less than 5% of the total energy. Immediately after the breaking wave, micro-vortices increase their strength absorbing energy from the mid-size vortices (15% of variation).

A closer look at turbulent energy dynamics can be obtained by analysing the spectra. The 1-D spectrum in the frequency domain is defined as the Fourier transform of the Eulerian time correlation:

$$E_1(f) = 2\overline{u'^2} \int_{-\infty}^{+\infty} f(t) e^{-i2\pi ft} dt \quad (22)$$

where $f(t)$ is the longitudinal time autocorrelation function. Using Taylor's hypothesis, we can transform the 1-D

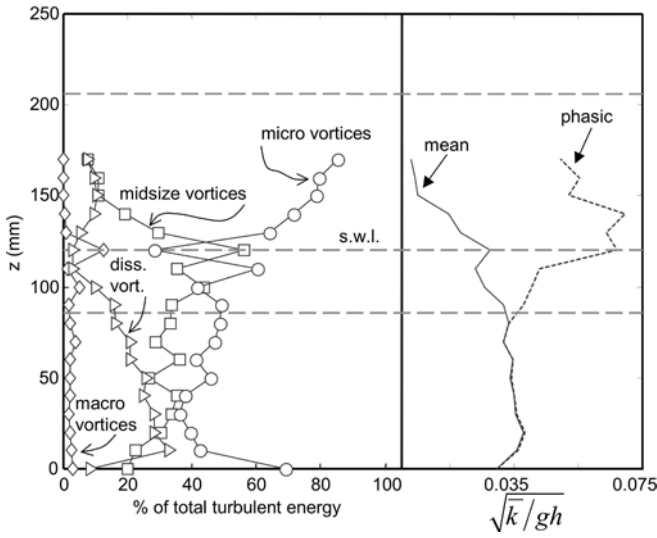


Fig. 8. Energy of different sizes vortices: dissipative vortices $l < 2$ mm (open right pointing triangle); micro-vortices $2 \text{ mm} < l < 0.10 \text{ m}$ (open circle); mid-size vortices $0.10 \text{ m} < l < 4.0 \text{ m}$ (open square) and macro-vortices $l > 4.0 \text{ m}$ (open diamond)

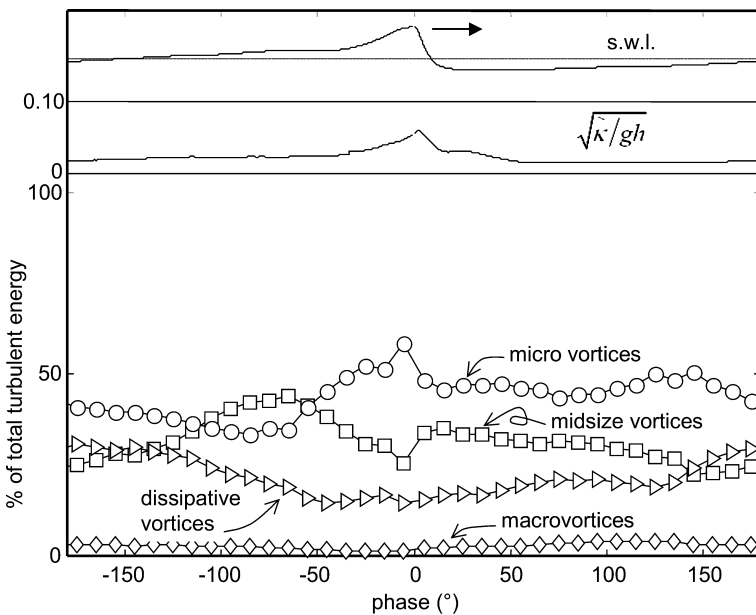


Fig. 9. Vertical averaged kinetic energy of different sizes vortices: dissipative vortices $l < 2$ mm (open right pointing triangle); micro-vortices $2 \text{ mm} < l < 0.10 \text{ m}$ (open circle); mid-size vortices $0.10 \text{ m} < l < 4.0 \text{ m}$ (open square) and macro-vortices $l > 4.0 \text{ m}$ (open diamond)

spectrum in the wave-number domain:

$$E_1(k_1) = \frac{U}{2\pi} E_1(f) \quad (23)$$

where k_1 is the wave-number component in the x direction. The 1-D spectrum satisfies the relation:

$$\overline{u'^2} = \int_0^{+\infty} E_1(f) df = \int_0^{+\infty} E_1(k_1) dk_1 \quad (24)$$

Using wavelet decomposition, we can evaluate the energy spectrum which is also resolved in phase. In Fig. 10 the 1-D measured spectra are presented, in non-dimensional form according to Kolgomorov. For easy interpretation only 90° phase resolution is adopted. For comparison, Pao's (1965) correlation is also plotted:

$$E(k) = \alpha \varepsilon^{2/3} k^{-5/3} \exp\left\{-\left(\frac{3\alpha}{2}\right)\left(\frac{k}{k_d}\right)^{4/3}\right\} \quad (25)$$

$E_1(k_1)$ can be expressed as:

$$E_1(k_1) = \alpha_1 \varepsilon^{2/3} k^{-5/3} \exp\left\{-\left(\frac{3\alpha_1}{2}\right)\left(\frac{k}{k_d}\right)^{4/3}\right\} \quad (26)$$

$\alpha \sim 3\alpha_1$ is the Kolgomorov constant and is about 1.5.

The most important variations during one wave cycle are in the wave-number band across the mid-size and the micro-vortices. At high wave number, the spectra collapse to a common form, as stated by Kolgomorov's first hypothesis on similarity, even though of different shape to the classical $-5/3$ equilibrium range form (in the inertial range). Pao's correlation is an attempt to model the dissipative-inertial range overlap. The discrepancy of present results with respect to the Pao's correlation at high wave numbers can be addressed to the filtering effect of the finite size of the volume of measurement. This effect should be present for $k/k_d > O(1)$.

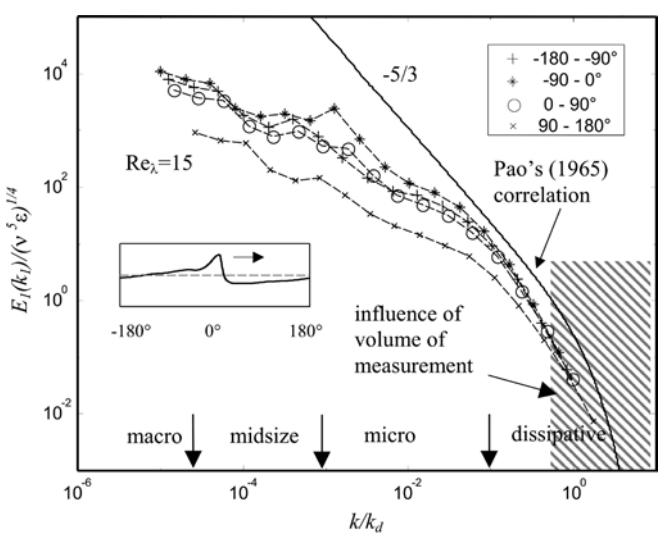


Fig. 10. One-dimensional Kolgomorov spectrum in wave-number domain. Measurements at the first level near the bottom

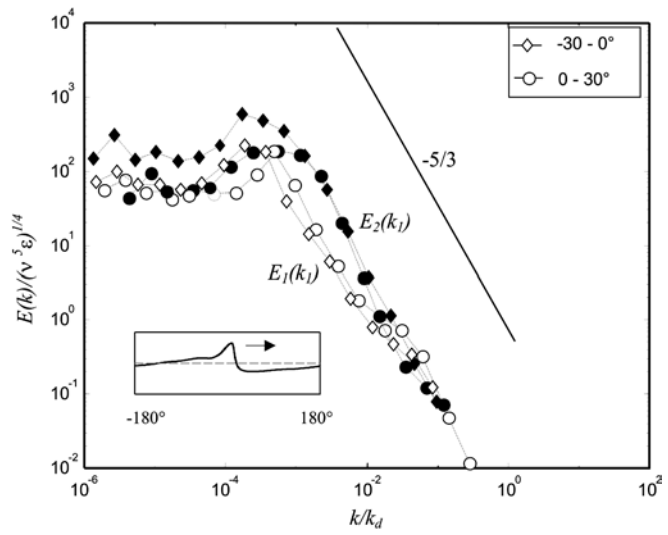


Fig. 11. One-dimensional spectra in wave-number domain. Measurements at $z=130$ mm over the bottom, in the wave crest

Figure 11 shows the energy spectra in the wave crest ($z=130$ mm) for the only two phases during which flow motion is detected. The spectra show a lack of energy in the low wave-number range, due to geometrical limitation: mid-size and macro-vortices cannot develop in the short time (and limited space) of the existence of the crest. Similar results are obtained for the energy spectrum $E_2(k_1)$, which is the cosine Fourier transform of the transverse velocity autocorrelation function:

$$E_2(k_1) = 2\overline{v'^2} \int_{-\infty}^{+\infty} g(x) e^{-ik_1 x} dx \quad (27)$$

and which is representative of the vertical turbulent energy. At higher wave number, the spectra measured at different phases for the two velocity components tend to collapse, as expected from the isotropy of small eddies. At

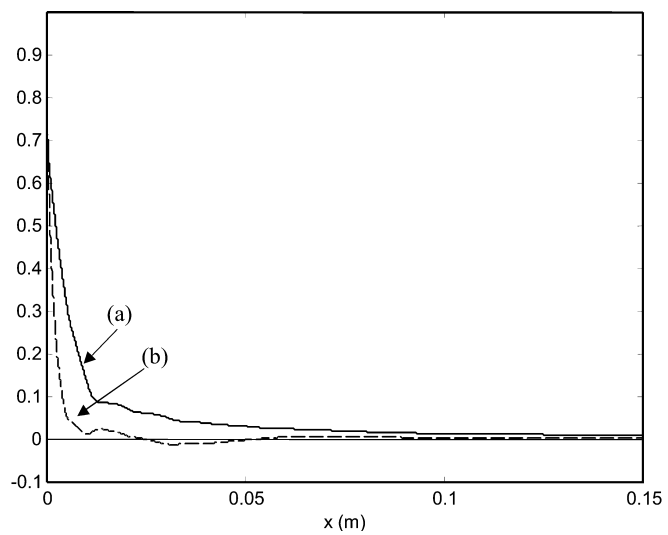


Fig. 12. Longitudinal (a) and transverse (b) correlation functions. Measurements at the first level near the bottom. Mean values during the wave period

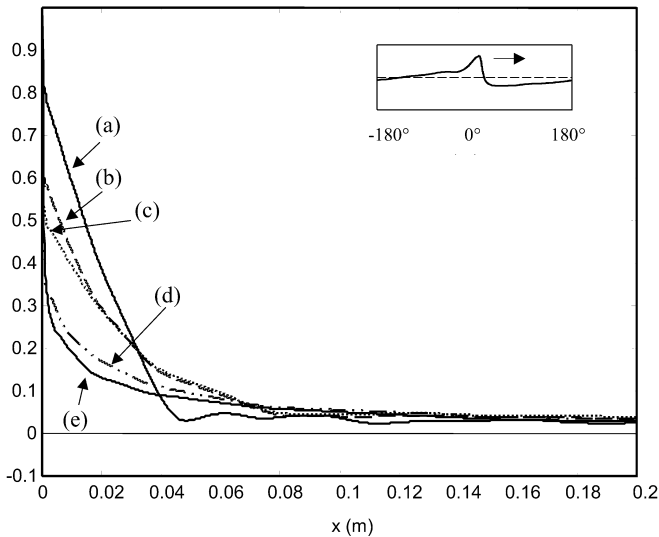


Fig. 13a-e. Phase variation of the computed longitudinal correlation function. a 15°; b 45°; c 75°; d 105°; e 145°. Measurements at $z=10$ mm

low wave numbers, a classical plateau confirms the absence of significant energy.

The inverse Fourier transforms of 1-D spectra are essentially the Eulerian time and Eulerian space autocorrelations. Knowledge of the form of the energy spectrum function $E_1(k_1)$ and $E_2(k_1)$ allows the computation of the autocorrelation functions $f(x)$ (longitudinal) and $g(x)$ (transverse). Figure 12 shows the longitudinal and transverse autocorrelation functions computed at the second level near the bottom, averaged over the entire wave cycle. They both have the typical shape generated by eddies of two distinct classes (see e.g. Townsend 1976, p. 20), with smaller eddies responsible for the fast decay below the vertex and bigger eddies responsible for the flat tail.

Using the spectra computed at different phases, the longitudinal correlation function has also been computed for each 30° phase band (Fig. 13). The time evolution of the function confirms the varying population of eddies during the wave cycle, which after wave breaking tends to the classical shape for turbulence with a wide spectrum of eddy size (curve e).

8

Conclusions

Turbulence in the immediate pre-breaking of laboratory spilling waves has been analysed using wavelet decomposition. The energy contribution at different eddy wave numbers and different phases during the wave cycle has been computed. Macro-vortices contain less than 5% turbulent energy, almost uniformly throughout the cycle. Micro-vortices and mid-size vortices contain an average of 70% of the energy, predominantly below the wave crest. Dissipation takes place at a varying rate, with almost 25% of the energy stored in eddies in the dissipative range.

The 1-D phase average energy spectrum is computed at different phases during the wave cycle. At high wave numbers it tends to the Kolmogorov equilibrium spectrum

as corrected by Pao (1965), with a constant $\alpha=1.5$ and with a probable discrepancy caused by the filtering effect of the finite volume of measurement. The main variation during the wave cycle refers to the wave-number band between the mid-size and micro-vortices, with a spike of energy during breaking.

Using the computed 1-D energy spectra, the longitudinal and transverse correlations were computed, either as an average over the wave cycle or at different phases. The eddy populations appear to be composed of two different wave-number bands. Also the varying population of eddies during wave cycle is described, with a progressive size reduction of macro-vortices.

References

- Batchelor GK (1953) The theory of homogeneous turbulence. Cambridge University Press, Cambridge
- Camussi R, Gui G (1997) Orthonormal wavelet decomposition of turbulent flows: intermittency and coherent structures. *J Fluid Mech* 348:177-199
- Chang K-A, Liu PL-F (1998) Velocity, acceleration and vorticity under a breaking wave. *Phys Fluids* 10:327-329
- Cox DT, Kobayashi N, Okayasu A (1994) Vertical variations of fluid velocities and shear stress in surf zones. In: Proceedings of the 24th International Conference on Coastal engineering. ASCE, Reston, Va., pp 98-112
- Dabiri D, Gharib M (1997) Experimental investigation of the vorticity generation within a spilling water wave. *J Fluid Mech* 330: 113-139
- Deigaard R, Fredsøe J, Hedegaard IB (1986) Suspended sediment in the surf zone. *J Waterway, Port, Coast Ocean Eng* 112:115-128
- Farge M (1992) Wavelet transforms and their applications to turbulence. *Ann Rev Fluid Mech* 24:395-457
- Foufoula-Georgiu E, Kumar P (eds) (1994) Wavelets in geophysics. In: Chui CK (series ed.) Wavelet analysis and its applications. Academic Press, New York
- Gabor D (1946) Theory of communication. *J Inst Elect Eng* 93:429-457
- George R, Flick RE, Guza RT (1994) Observation of turbulence in the surf zone. *J Geophys Res* 99(C1):801-810
- Gilliam X, Duniak J, Doggett A, Smith D (2000) Coherent structure detection using wavelet analysis in long time-series. *J Wind Eng Indust Aerodyn* 88:183-195
- Greared CA, Emarat N (2000) Optical studies of wave kinematics. In: Liu PL-F (ed.) Advances in coastal and ocean engineering, vol 6. World Scientific, Singapore
- Hajji MR (1999) Intermittency of energy containing scales in atmospheric surface layer. *J Eng Mech ASCE* 125:797-803
- Hajji MR, Tieleman HW, Tian L (2000) Wind tunnel simulation of time variations of turbulence and effects on pressure on surface-mounted prisms. *J Wind Eng Ind Aerodyn* 88:197-212
- Hattori M, Aono T (1985) Experimental study on turbulence structures under spilling breakers. In: Toba H, Mitsuyasu H (eds) The ocean surface. Reidel, Dordrecht, pp 419-424
- Hinze JO (1975) Turbulence. McGraw-Hill, New York
- Hudgins L (1992) Wavelet analysis of atmospheric turbulence. Ph.D. Thesis, University of California, Irvine, Calif.
- Kaspersen JH, Krostad P-Å (2001) Wavelet-based method for burst detection. *Fluid Dynam Res* 28:223-236
- Kolmogorov AN (1962) A refinement of previous hypotheses concerning the local structure in a viscous incompressible fluid at high Reynolds number. *J Fluid Mech* 13:82-85
- Longo S, Losada IJ, Petti M, Pasotti N, Lara J (2001) Measurements of breaking waves and bores through a USD velocity profiler. Technical Report UPR/UCa_01_2001, University of Parma, University of Santander
- Longo S, Petti M, Losada IJ (2002) Turbulence in the surf zone and in the swash zone: a review. *Coastal Eng* 45:129-147
- Lin J-C, Rockwell D (1994) Instantaneous structure of a breaking wave. *Phys Fluids* 6:2877-2879

- Liu PC (2000) Wavelet transform and new perspective on coastal and ocean engineering data analysis. In: Liu PL-F (ed.) *Advances in coastal and ocean engineering*, vol 6. World Scientific, Singapore
- Mallat S (1989) A theory for multiresolution signal decomposition: the wavelet representation. *IEEE Trans Pattern Anal Machine Intell* 11:674–693
- McComb WD (1990) *The physics of fluid turbulence*. Oxford University Press, Oxford
- Nadaoka K, Kondoh T (1982) Laboratory measurements of velocity field structure in the surf zone by LDV. *Coastal Eng Japan* 25:125–145
- Nadaoka K, Hino M, Koyano Y (1989) Structure of the turbulent flow field under breaking waves in the surf zone. *J Fluid Mech* 204:359–387
- Newland DE (1993) *Random vibrations, spectral analysis and wavelet analysis*, 3rd edn. Prentice Hall, Englewood Cliffs, N.J.
- Obukhov AM (1962) Some specific features of atmospheric turbulence. *J Fluid Mech* 13:77–81
- Pao YH (1965) Structure of turbulent velocity and scalar fields at large wavenumbers. *Phys Fluids* 8:1063–424
- Petti M, Longo S (2001) Turbulence experiments in the swash zone. *Coastal Eng* 43:1–24
- Rodriguez A, Sanchez-Arcilla A, Redondo JM, Mosso C (1999) Macroturbulence measurements with electromagnetic and ultrasonic sensors: a comparison under high-turbulent flows. *Exp Fluids* 27:31–42
- Sakai T, Inada Y, Sandanbata I (1982) Turbulence generated by wave breaking on beach. In: *Proceedings of the 18th International Conference on Coastal engineering*. ASCE, Reston, Va., pp 3–21
- Stive MJF (1980) Velocity and pressure field of spilling breakers. *Proceedings of the International Conference on Coastal engineering*. ASCE, Reston, Va., pp 547–566
- Svendsen IA (1987) Analysis of surf zone turbulence. *J Geophys Res* 92:5115–5124
- Svendsen IA, Putrevu U (1995) Surf zone hydrodynamics. Research Report No. CACR-95-02, University of Delaware
- Tennekes H, Lumley JL (1972) *A first course in turbulence*. The MIT Press, Cambridge, Mass.
- Thornton EB (1979) Energetics of breaking waves in the surf zone. *J. Geophys Res* 84:4931–4938
- Ting CKF, Kirby JT (1994) Observation of undertow and turbulence in a laboratory surf-zone. *Coastal Eng* 24:51–80
- Ting CKF, Kirby JT (1995) Dynamics of surf-zone turbulence in a strong plunging breaker. *Coastal Eng* 24:177–204
- Ting CKF, Kirby JT (1996) Dynamics of surf-zone turbulence in a spilling breaker. *Coastal Eng* 27:131–160
- Townsend AA (1976) *The structure of turbulent shear flow*. Cambridge University Press, Cambridge
- Ville J (1948) Théorie et applications de la notion de signal analytique. *Câbles Transmission* 2:61–74
- Wigner EP (1932) Quantum correction for thermodynamic equilibrium. *Phys Rev* 40:749–759